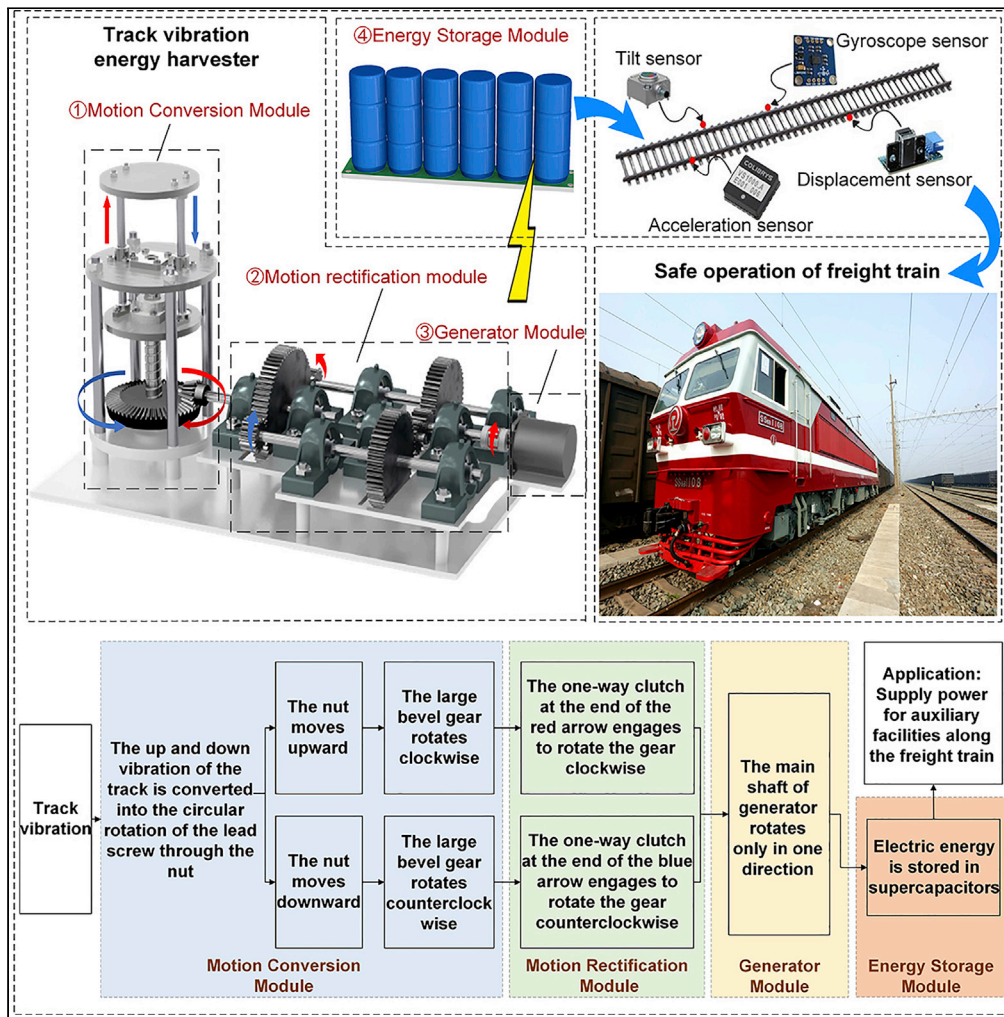## Article

A vibration energy harvester for freight train track self-powered application

Genshuo Liu,
Zheng Fang,
Zutao Zhang, ...,
Xiaoping Wu,
Zhou Jin,
Dongyang Li

zzt@swjtu.edu.cn

Highlights

A track vibration energy harvester is designed for applications in freight trains

A ball screw is used to convert the bidirectional motion to unidirectional rotations

Using bevel gear to increase the speed can maximize the use of the track input force

The maximum output power and mechanical efficiency are 28.0416W and 75.92%

Article

A vibration energy harvester for freight train track self-powered application

Genshuo Liu,[1,2] Zheng Fang,[1,2] Zutao Zhang,[1,2,4,*] Xing Tan,[1,2] Chutian Dai,[1,2] Xiaoping Wu,[1,2] Zhou Jin,[3] and Dongyang Li[3]

SUMMARY

The safe and stable operation of the widely distributed freight trains urgently needs to solve the power supply problem of the freight train track monitoring network. In this article, an innovative and efficient energy harvesting mechanism is designed based on a mechanical vibration rectifier (MVR), with four modules of motion conversion, motion rectification, generator, and storage. The motion conversion module converts the linear vibration of the rail into rotational motion through the ball screw. The motion rectification module integrates mechanical rectification and transmission speed-up and converts the bidirectional rotation of the transmission shaft into a faster unidirectional rotation of the generator. Experiments show that the power and mechanical efficiency of the proposed vibration energy harvester can reach 28.0416W and 75.92%, respectively. This high-performance MVR can meet the power demand of wireless sensor networks by harvesting vibration energy to ensure the normal operation of freight trains.

INTRODUCTION

Freight trains are widely distributed, but rail safety issues during transportation are not guaranteed. Low-power wireless sensing devices are increasingly being used to monitor track safety, but the energy supply for these sensors is a thorny issue (Cañete et al., 2015; Hodge et al., 2015; Jin et al., 2017; Liu et al., 2018; Zhao et al., 2017). The cost of transmitting electricity over long distances is prohibitive in areas with power shortages. It is difficult to ensure a normal power supply even because of harsh natural environment factors such as rugged terrain and changeable weather. If batteries are used to power these electronic devices, they can only meet the electricity demand for a short period and require regular manual maintenance. Not only is it a waste of human resources but these discarded batteries may also pollute the environment (Hao et al., 2022; Schismenos et al., 2021). Environmental energy recovery technology can realize the self-powered of wireless monitoring nodes green and cleanly. Solar energy, wave energy, wind energy, noise energy, and vibration energy are all part of environmental energy. Among them, solar energy is greatly affected by weather and seasons and cannot provide a continuous and stable energy supply (Yu et al., 2022). Wind and wave energy are too dependent on terrain and region to ensure the universality of energy harvesting installations (Abido et al., 2022; Xie et al., 2020). The noise power generation is too low to fully meet the needs of wireless sensor devices (Wang et al., 2018). Vibration energy is a widespread energy beam, such as rails, wheels, bridges, etc (Cao et al., 2022; Park, 2017). Especially for the track vibration, the running speed of the train, the load, the unevenness of the track, the mismatch between the track and the wheels, etc., will cause and excite the track to different degrees of strong vibration (Qi et al., 2022). And the track vibration has strong adaptability to environmental conditions such as weather and temperature. Therefore, it is necessary to develop a high-performance rail vibration energy harvester to meet the electricity demand of low-power sensor devices, to ensure the safe and stable operation of freight trains.

Because of the higher power generation and the need for no external power supply, some scholars have studied electromagnetic vibration energy harvesters. Pourghodrat proposed to improve the original harvester's shortcomings of being unable to harvest upward vibration (Pourghodrat et al., 2014,2011). The improved model consists of gears, racks, and a pair of clutches. The test connected a resistor with a total resistance of 131Ω in series with the generator and obtained the output voltage on the 10Ω resistor. Experiments were carried out on the rotation speed of the generator under the conditions of no-load (120 rpm) and loaded (560 rpm) trains, respectively. Under no-load and load conditions, the average output power

[1]School of Mechanical Engineering, Southwest Jiaotong University, Chengdu 610031, PR. China

[2]Yibin Research Institute, Southwest Jiaotong University, Yibin 644000, PR. China

[3]China Railway Wuhan Electrification Bureau Group Shanghai Electric Co., Ltd, Shanghai 201799, PR. China

[4]Lead contact

*Correspondence: zzt@swjtu.edu.cn

https://doi.org/10.1016/j.isci.2022.105155

increased to 0.19 and 4.24W. Gao (Gao et al., 2016) et al. designed a copper-bead spaced track-type electromagnetic energy harvester, which is suitable for freight trains to capture energy caused by vibrations between the wheel pair and the track system. Using copper beads as radial spacing ensures reliable unidirectional motion of the magnets inside a multilayer-multirow coil. The magnetic levitation harvester can capture vibrations in the low-frequency range of 3–7 Hz with an amplitude of 0.6–1.2 mm. For the resonance harvest, the output power is 119 mW for a displacement of 1.2 mm load resistance of 44.6 Ω. A fast anchor-free installation of an energy harvester for freight trains was presented by Lin (Lin et al., 2018) et al. For the protection of the track structure, the energy harvester is held in place using a combination of spring preload and a reset device. Although the freight train was in operation, tests on the harvester showed a mean output of 7W at a vibration amplitude of 5.7 mm and a travel speed of 64 km/h. Pan proposed a rack-pinion pinion-based suspension energy harvester with a simplified structure (Pan et al., 2019b). They also designed an enclosed lubricated gearbox and a unique two-guide-rail mechanism specifically for the harvester. The onboard test with the gearbox ratio of 43:1 was tested, and the average power was 1.3 W when the total weight of the load was about 23 tons, and the speed was 30 km/h. Zhang designed a heavy-duty freight railway harvester based on a scissor link and slider mechanism (Zhang et al., 2022). The bench test for mechanical testing and sensing machine testing was performed with a maximum output power of 7.44W at an amplitude of 8 mm, a frequency of 4Hz, and an external resistance of 2Ω.

However, there are still many problems in the research of electromagnetic track vibration energy harvesters. (1) The installation of the device will cause structural changes to the track facilities, which may cause hidden dangers to the safe operation of freight trains; (2) the energy harvester has low power generation and does not fully take advantage of the large input force of track vibration, and cannot fully cover the energy consumption of the wireless sensor system (Kim et al., 2019); (3) the reasonableness of the design, the processing accuracy of the device and the production cost, and the service life are subject to improvement (Jin et al., 2015). This article proposes a novel electromagnetic track vibration energy harvester based on mechanical vibration rectifier (MVR). The device is installed on the underside of the track between the two sleepers and does not cause damage to the track structure. The proposed system includes a motion conversion module, a motion rectification module, a generator module, and an energy storage module. The ball screw is used as the motion input mechanism of the device, and the motion rectification module performs mechanical rectification and increases speed. The reciprocating vibration becomes unidirectional rotational motion after rectification and acceleration, and the mechanical energy is converted into electrical energy by the generator, which is finally stored in the supercapacitor. The acceleration ratio of the device reaches 1:48, which fully uses the large force of the track vibration caused by the freight train to increase the power generation of the energy harvester, thereby meeting the power supply demand of the wireless sensor. The energy harvester proposed in this article can not only solve the high cost of laying the power grid but also reduce the pollution of the battery to the environment. In some remote, severe cold, plateau, and other harsh environments, it provides a continuous energy supply for the wireless sensor platform to ensure the safe operation of freight trains.

System design

During the running of freight trains, their body weight is heavier than that of ordinary trains because of their cargo capacity. Therefore, the track can also generate more severe vibration during the running process, which leads to the dissipation of a large part of the mechanical energy. Besides, the lack of energy supply for the auxiliary monitoring facilities of most freight trains during running. Therefore, a track vibration energy harvesting device integrating motion conversion and motion rectification modules is proposed. Self-power supply for the electrical equipment connected to the freight train tracks includes traffic lights, track quality and safety monitoring sensors, and other auxiliary facilities. As shown in Figure 1, the track vibration energy harvesting device includes four modules: A motion conversion module, a motion rectification module, a generator module, and an energy storage module. The motion conversion module transmits track vibration and converts linear reciprocating motion into bidirectional rotational motion. The motion rectification module has speed boosting and mechanical rectification functions. A brushless generator is used as the electrical output device. In practical applications, the generated electrical energy is rectified and stabilized and finally stored in the supercapacitor.

Motion conversion module

Figure 2 illustrates the structure of the motion conversion module used to harvest the vertical vibration response of the track. The energy conversion module includes two single-degree-of-freedom motion input boards, two fixed boards, four fixed shafts, a set of right-handed ball screw, and a large bevel gear. The
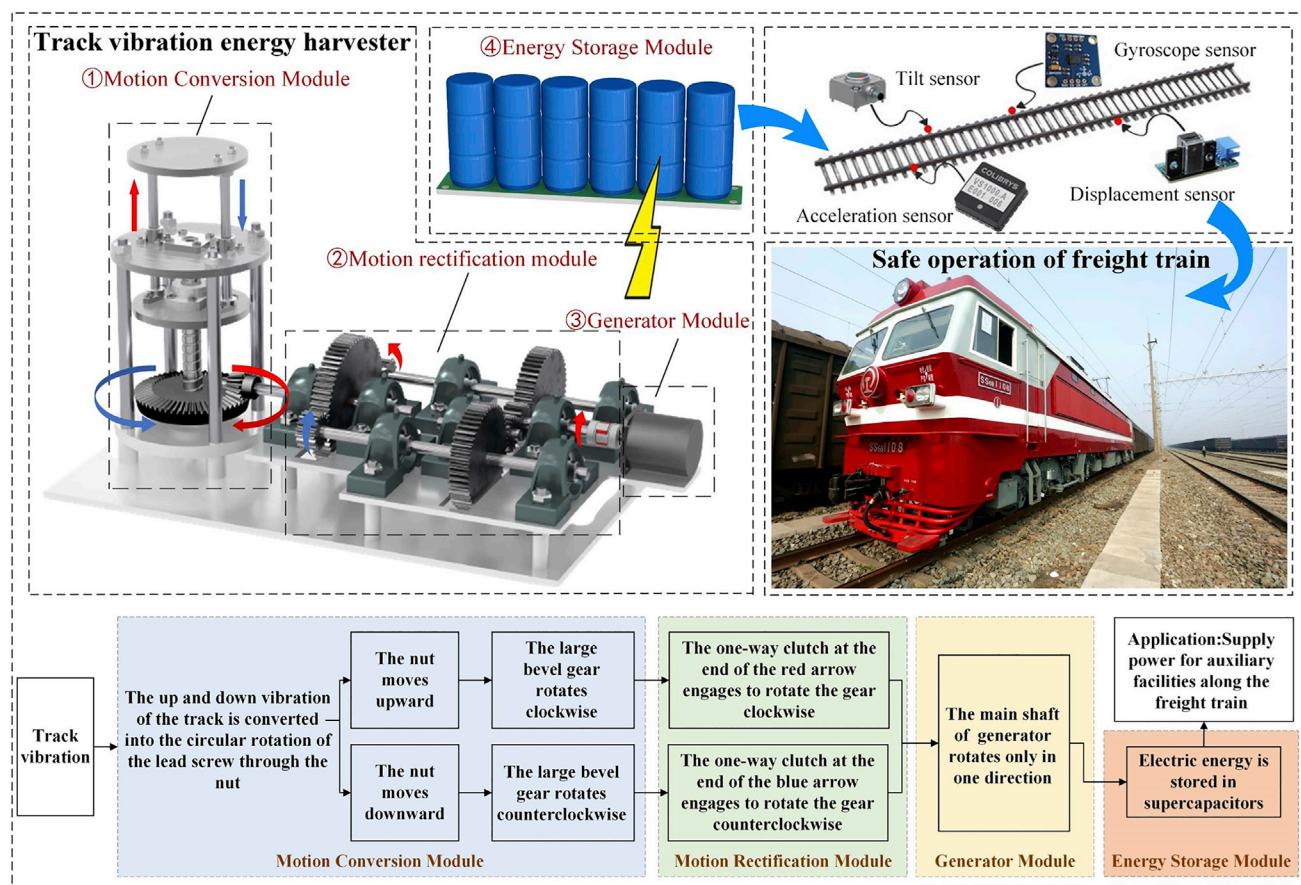
Figure 1. Structure of a kinetic energy harvester based on mechanical vibration rectifier

upper input board harvests the track vibration through the shaft holders, the linear sliding circular flange bearing, and the two support shafts. When the track is in contact with the upper input board, the input boards move the nut downwards and the lead screw drives the large bevel gear to rotate counterclockwise. When the speed is 0 mm/s, the upper input board moves upward in the opposite direction. At this time, the nut moves upwards and the lead screw drives the large bevel gear to rotate clockwise. The up and down movement of the nut causes the lead screw to make a reciprocating rotational movement, thus achieving the same reciprocating rotational movement of the large bevel gear. The motion of the entire process is transformed from the linear vibration input of the track to rotational motion. Finally, the motion is transmitted to the motion rectification module by meshing large and small bevel gears.

Motion rectification module

As shown in Figure 3, the motion rectification module is the key part of the energy harvester, increasing the transmission speed and mechanical rectification. The core of the motion rectification section is the one-way bearing in gear ① and gear ③. The two one-way bearings are placed in the inner holes of gear ① and gear ③ with opposite meshing directions. They are connected with gears ① and ③ by welding. This is significant because the transmission shaft meshes with gear ① and gear ③ in opposite directions, respectively. When gear ② is turned clockwise, the internal one-way bearing of gear ① transmits the torque and is responsible for the motion transmission. At this time, the internal one-way bearing of gear ③ is in the overrun state and does not transmit torque. After two-stage gear acceleration, the rotation is transmitted to the generator shaft, causing the generator shaft to rotate clockwise. When gear ② rotates counterclockwise, the internal one-way bearing of gear ③ transmits torque and is responsible for motion transmission. At this time, the internal one-way bearing of gear ① is in the overrun state and does not transmit torque. Then after two-stage gear acceleration, the rotation is transmitted to the generator shaft, which still rotates in a clockwise direction. Gear ⑤ is an idler gear, which in addition to changing the direction, also plays a role in satisfying
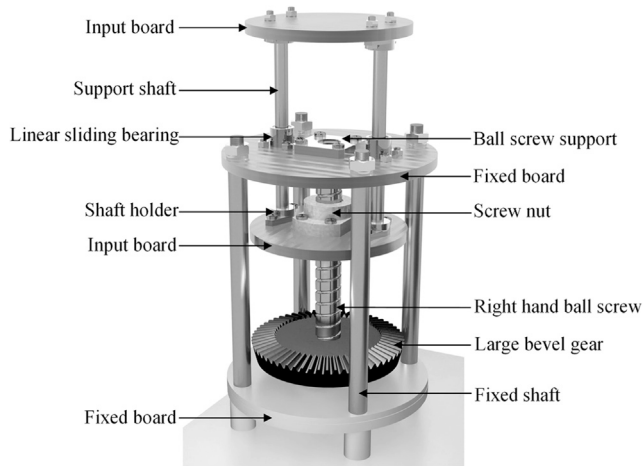
Figure 2. Motion conversion module

the arrangement of the entire transmission system by extending the wheelbase. It also has a certain energy storage effect, which contributes to the stability of the system. The bidirectional rotation of the input is converted into unidirectional rotation of the output using a motion rectification module. This significantly increases the degree of energy harvesting compared to bidirectional rotation and improves the harvesting efficiency and reliability of the system. Finally, the conversion of the bidirectional reciprocating motion of the track to the unidirectional rotational motion of the shaft of the generator is realized.

Generator module

The unidirectional rotation generated by the motion rectification module can be converted into electrical energy by the generator module. To improve the power generation efficiency and facilitate installation, the generator should have the characteristics of small rotational inertia, small copper loss and small size (Li et al., 2022; Zhang et al., 2022). Therefore, the generator (57BL55S06- 230TF9) is selected in this article, as shown in Figure 4. The detailed parameters of the generator are shown in Table 1.

Energy storage module

Because the brushless generator used in this article produces a three-phase alternating current, it cannot directly store or supply power to the load. Therefore, as shown in Figure 4, a three-phase bridge rectifier
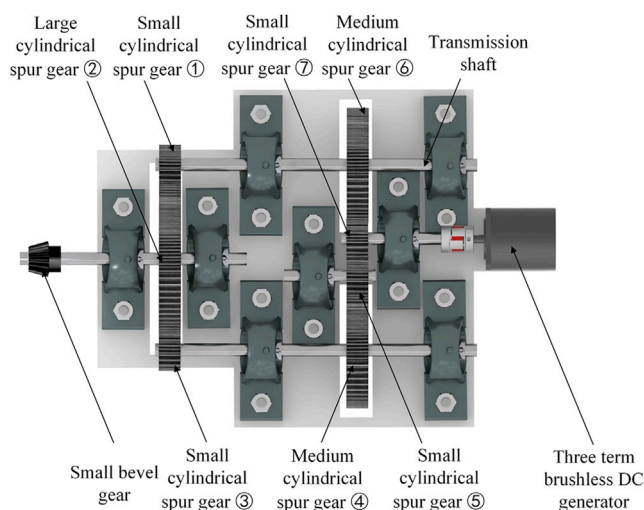

Figure 3. Motion rectification module

A

Three-phase generator | Rectifier module | Super-capacitor

Rectifier voltage regulator circuit

B

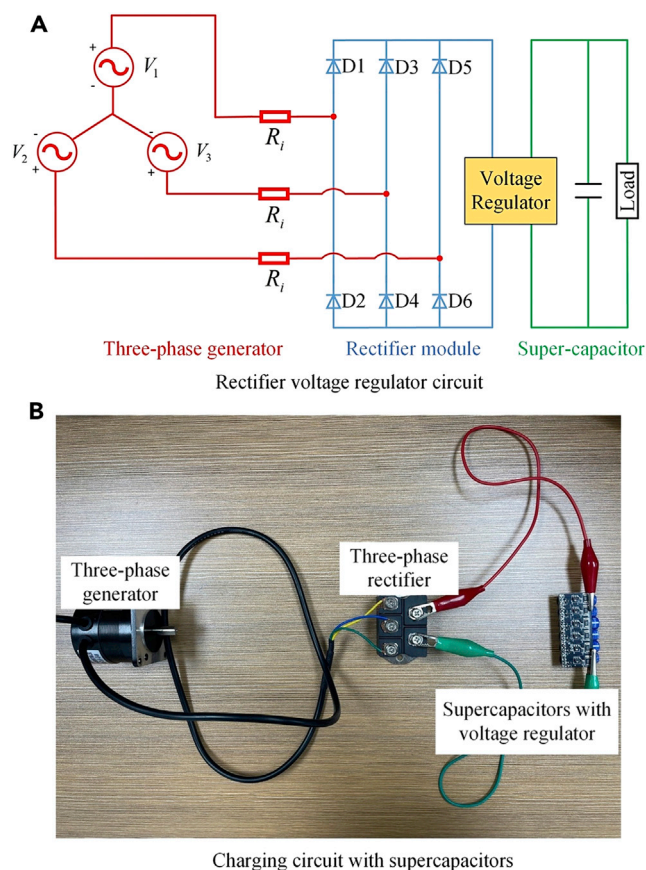Charging circuit with supercapacitors

Figure 4. Electric circuit of the energy storage module
(A) Rectifier voltage regulator circuit.
(B) Charging circuit with supercapacitors.

circuit converts three-phase alternating current into direct-current pulse current. Then, the generator excitation current is controlled by the voltage regulator, and the output voltage is adjusted to a constant value. So that it can stably and continuously supply power to the load. Compared with batteries, supercapacitors have excellent cycle stability, large energy storage capacity, high power density, extremely fast charging and discharging speed, high energy conversion efficiency, long service life, strong temperature performance, and high safety factor. Considering the particularity of the freight train track environment, the energy storage elements are required to have a longer working life, stronger temperature adaptability, and larger energy storage space. Therefore, supercapacitors are chosen as energy storage elements.

Dynamic analysis and simulation

This section carries out the dynamic analysis of the MVR to establish the mathematical model of the device and analyze the dynamic characteristics of the device. Modeling the device can provide a theoretical basis for subsequent simulations and experiments, as shown in Figure 5. This articles proposes a freight train track vibration energy harvester with a ball screw as the core conversion component. Different from the traditional linear energy harvesting device of the track, the MVR takes full advantage of the large input force by adding a set of speed-increasing bevel gears. Continue to increase the speed in the spur gear transmission and convert the reciprocating linear vibration of the track into the unidirectional rotation of the generator through the one-way bearing, which further improves the power generation performance of the MVR. When the small cylindrical spur gear and the transmission shaft are relatively stationary, the one-way bearing engages with the transmission shaft to transmit the torque and drives the generator to rotate unidirectionally.

On the contrary, when the rotation speed of the small cylindrical spur gear is lower than that of the transmission shaft, the one-way bearing is idling and does not transmit motion torque. At this time, the one-way bearing on

Table 1. Parameters of the generator module

Parameters	Value
Rated voltage	24V
Rated current	3.6A
Rated power	60W
Rated torque	600N·mm
Rated speed	1000rpm
Max permissible speed	3500rpm
Internal resistance	1.15Ω
Inductance	1.9×10^{-3}H
Back EMF constant	0.060V·s/rad

the other side is in the meshing state, so the two sides mesh alternately. In this way, the continuity of the movement is ensured, and mechanical rectification and acceleration are realized at the same time.

Analysis of rotation damping coefficient of generator

As shown in Figure 6, the three windings of the brushless generator are connected in a star shape. The resulting AC will have a phase difference of 120°. The three-phase voltage of the generator can be expressed as:

$$\begin{cases} V_1 = E_m \cdot sin(\omega_S t) \\ V_2 = E_m \cdot sin\left(\omega_S t - \frac{2}{3}\pi \right) \\ V_3 = E_m \cdot sin\left(\omega_S t + \frac{2}{3}\pi \right) \end{cases}$$

(Equation 1)

where, V_1, V_2, and V_3 are the phase voltages of the generator;

E_m and ω_S represent the amplitude and angular frequency of the induced voltage.

The power P_C that can be recovered in the circuit and the power P_I caused by the internal resistance consumption constitutes the electromagnetic power P_E of the generation, P_E can be expressed as:

$$P_E = P_C + P_I = \frac{V_1{}^2}{R_e + R_i} + \frac{V_2{}^2}{R_e + R_i} + \frac{V_3{}^2}{R_e + R_i}$$

(Equation 2)

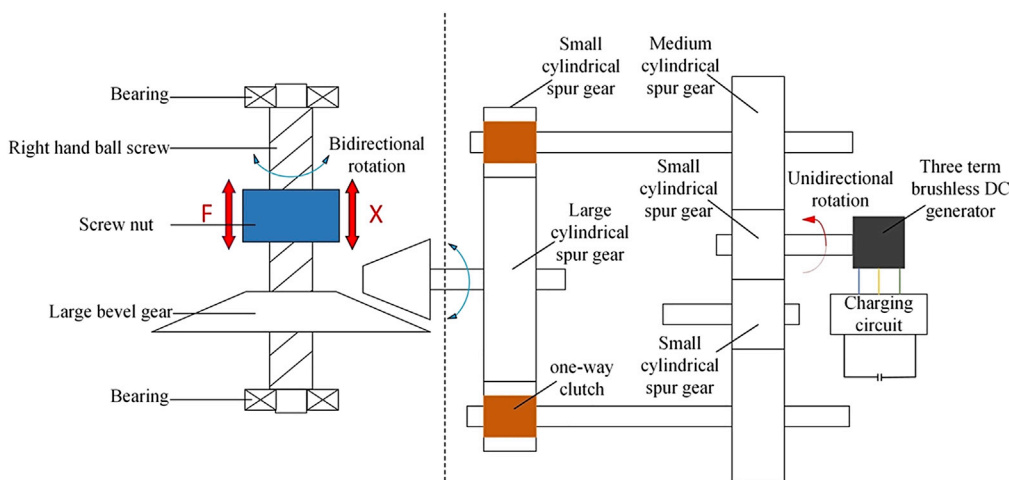where, the internal resistance of the generator is denoted by R_i;

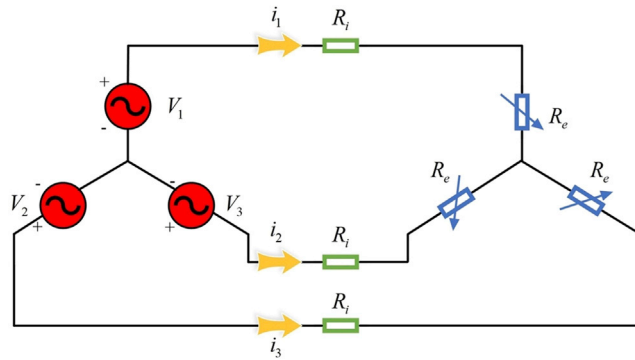**Figure 5. The dynamic model of the proposed track MVR harvester**

Figure 6. Schematic diagram of the three-phase DC generator energy feed circuit

the variable external equivalent resistance is denoted by R_e.

and P_C can be represented as:

$$P_C = \frac{V_1{}^2 \cdot R_e}{R_e + R_i} + \frac{V_2{}^2 \cdot R_e}{R_e + R_i} + \frac{V_3{}^2 \cdot R_e}{R_e + R_i} \qquad \text{(Equation 3)}$$

The electromagnetic efficiency η_e of the device can be expressed as:

$$\eta_e = \frac{P_C}{P_C + P_l} = \frac{R_e}{R_e + R_i} \qquad \text{(Equation 4)}$$

Combining Equation (1) with Equation (2), the electromagnetic power can be expressed as:

$$P_E = \frac{1.5 \times E_m{}^2}{R_e + R_i} \qquad \text{(Equation 5)}$$

At the same time, the amplitude E_m of the induced voltage can be obtained from the angular velocity ω_g of the generator shaft and the back EMF constant k_e, which is expressed as follows:

$$E_m = k_e \cdot \omega_g \qquad \text{(Equation 6)}$$

Substituting Equation (6) into Equation (5), the electromagnetic power P_E can be simplified as:

$$P_E = \frac{1.5 \times k_e{}^2 \cdot \omega_g{}^2}{R_e + R_i} \qquad \text{(Equation 7)}$$

Because of the conservation of energy, the electromagnetic power P_E is also expressed as:

$$P_E = T_E \cdot \omega_g \qquad \text{(Equation 8)}$$

where, the electromagnetic torque of the generator shaft is denoted by T_E.

The electromagnetic torque of the generator shaft is linearly related to the angular velocity of the shaft, which can be expressed as follows:

$$T_E = C_R \cdot \omega_g \qquad \text{(Equation 9)}$$

where, the generator rotation damping coefficient is denoted by C_R.

Combining Equation (8) with Equation (9), the electromagnetic power can be expressed as:

$$P_E = C_R \cdot \omega_g{}^2 \qquad \text{(Equation 10)}$$

The expression of the generator rotation damping coefficient C_R can be derived from Equations (7) and (10):

$$C_R = \frac{1.5 \times k_e{}^2}{R_e + R_i} \qquad \text{(Equation 11)}$$

This equation shows that the generator rotation damping coefficient is proportional to the back EMF constant k_e and inversely proportional to the total circuit resistance (R_e, R_i).

Linear damping coefficient analysis

From the law of conservation of energy, it is clear that the input system power P_{input} is equal to the sum of the power lost by the system P_f and the electromagnetic power P_E of the generator. The power lost by the system is mainly divided into four parts: ball screw, bevel gear, spur gear, and generator loss power.

$$P_{input} = P_f + P_E \qquad \text{(Equation 12)}$$

$$P_E = \eta_{bs} \cdot \eta_b \cdot \eta_{sg} \cdot \eta_g \cdot P_{input} = \eta \cdot P_{input} \qquad \text{(Equation 13)}$$

where, the transmission efficiency of the ball screw is denoted by η_{bs};

the transmission efficiency of the bevel gears is denoted by η_b;

the transmission efficiency of the spur gear system is denoted by η_{sg};

the mechanical efficiency of the generator is denoted by η_g;

the total transmission efficiency is denoted by η.

Because in the following friction analysis, the friction generated by the interaction of various mechanical components such as ball screws, bevel gear assembly, spur gear meshing, bearings, etc., has been considered in the MVR system. These are the same as the total loss efficiency η. Here we set the total transmission efficiency $\eta = 1$ because we will introduce the friction F_f into the overall system dynamics analysis later.

The input power of the MVR can be expressed as:

$$P_{input} = C_L \cdot \dot{x}^2 \qquad \text{(Equation 14)}$$

where, C_L is the linear damping of the MVR;

$\dot{x}$ is the velocity of the input board.

Substitute Equations (10) and (14) in turn into Equation (13), we can get:

$$\eta \cdot C_L \cdot \dot{x}^2 = C_R \cdot \omega_g{}^2 \qquad \text{(Equation 15)}$$

Linear motion can be converted into rotary motion using a ball screw, and the conversion equation is:

$$\omega = \frac{2\pi \cdot \dot{x}}{l} \qquad \text{(Equation 16)}$$

where, the rotational angular velocity of the ball screw is denoted by ω;

the lead of the ball screw is denoted by l.

$$\omega_g = i \cdot \omega \qquad \text{(Equation 17)}$$

where, $i = i_1 \cdot i_2 \cdot i_3$;

the shaft angular velocity of the generator is denoted by ω_g;

the transmission ratio of the bevel gears is denoted by i_1;

the transmission ratio of the spur gear system is denoted by i_2、 i_3;

the total transmission ratio is denoted by.

Combining Equations (16) and (17) with Equation (15) gives an expression for the linear damping coefficient C_L of the MVR.

$$C_L = \frac{6\pi^2 i^2 k_e^{\,2}}{(R_e + R_i)\cdot l^2 \cdot \eta} \qquad \text{(Equation 18)}$$

The above equation shows that the linear damping coefficient C_L of the MVR is proportional to the total transmission ratio and the back EMF constant of the generator; it is inversely proportional to the total loss efficiency, the lead of the ball screw, and the total circuit resistance.

Friction analysis

In the MVR structure, the friction generated by the interaction of various mechanical components such as ball screws, bevel gear assembly, spur gear meshing, and bearings is the main cause of power loss. The literature (Penalba, 2018) proposes that oversimplification of the MVR model can lead to an incorrect assessment of total power absorption during modeling and analysis. The frictions from the different components of the MVR are combined into one term and expressed using the following Equation (Armstrong-Hélouvry et al., 1994; Dupont et al., 2002; Li et al., 2020):

$$F_f = \begin{cases} F_C + (F_S - F_C)e^{\left(\frac{v}{V_S}\right)^2} + C_v v, & v \neq 0 \\ F_e, & v = 0 \end{cases} \qquad \text{(Equation 19)}$$

where F_f, F_C, F_S, C_v, and F_e are the total friction, the Coulomb friction, the Stribeck friction, viscous friction coefficient, and maximum static friction, and v and V_s are the velocity of the MVR and the relative velocity threshold for the Stribeck friction. When the MVR is still, the static friction can be any value less than F_e, depending on the value of the actuating force. The unknown term in the expression for total friction F_f can be obtained by measuring the force required by the MVR system in the open circuit state without any external resistance and using the mathematical least squares method.

Kinetic analysis

The MVR generates a displacement x under the action of the excitation force F_1, and the mathematical description of the vibration system can be obtained by the Lagrangian equation as follows:

$$\frac{d}{dt}\left(\frac{\delta T}{\delta \dot{x}}\right) - \frac{\delta T}{\delta x} + \frac{\delta V}{\delta x} + \frac{\delta D}{\delta \dot{x}} = F_1 \qquad \text{(Equation 20)}$$

where, the kinetic energy of the MVR is denoted by T;

the dissipation function of the MVR is denoted by D.

When the one-way bearings transmit torque, the equation of motion is as follows:

$$\frac{d\theta_{in}}{dt} = \frac{d\theta}{dt} \qquad \text{(Equation 21)}$$

where, the angle of rotation of the ball screw is denoted by θ_{in};

the angle of rotation when the one-way bearing is engaged is denoted by θ.

The angular velocity ω of the ball screw in the motion conversion module can be expressed as follows:

$$\omega = \frac{d\theta_{in}}{dt} = \frac{2\pi \cdot \dot{x}}{l} \qquad \text{(Equation 22)}$$

The kinetic energy T of the input transmission system can be expressed as the sum of the kinetic energy of the reciprocating part and the kinetic energy of the rotating part.

$$T = \frac{1}{2}\cdot m_c \cdot \dot{x}^2 + \frac{1}{2}\cdot J_S \cdot \omega^2 + \frac{1}{2}\cdot J_{lb}\cdot \omega^2 + \frac{1}{2}\cdot J_{sb}\cdot (i_1\omega)^2 + \frac{1}{2}\cdot J_{lg}\cdot (i_1\omega)^2$$
$$+ J_{sg1}\cdot (i_1 i_2 \omega)^2 + J_{mg}\cdot (i_1 i_2 \omega)^2 + J_{sg2}\cdot (i_1 i_2 i_3 \omega)^2 + \frac{1}{2}\cdot J_g \cdot (i_1 i_2 i_3 \omega)^2 \qquad \text{(Equation 23)}$$

where, the total mass of objects in reciprocating motion is m_c;

inertia of ball screw is J_S;

inertia of large bevel gear is J_{lb};

inertia of small bevel gear is J_{sb};

inertia of large cylindrical spur gear ② is J_{lg};

inertia of small cylindrical spur gears ① and ③ is J_{sg1};

inertia of medium cylindrical spur gears ④ and ⑥ is J_{mg};

inertia of small cylindrical spur gears ⑤ and ⑦ is J_{sg2};

rotational inertia of generator is J_g.

Substituting Equation (22) into Equation (23), the kinetic energy T of the MVR can be obtained:

$$T = \frac{1}{2}\dot{x}^2 \cdot \left[m_c + \frac{4\pi^2 \left(J_S + J_{lb} + J_{sb}i_1{}^2 + J_{lg}i_1{}^2 + 2J_{sg1}i_1{}^2 i_2{}^2 + 2J_{mg}i_1{}^2 i_2{}^2 + 2J_{sg2}i^2 + J_g i^2 \right)}{l^2} \right] \quad \text{(Equation 24)}$$

The MVR dissipation function can be expressed using the Rayleigh dissipation function:

$$D = \frac{1}{2} \cdot C_L \cdot \dot{x}^2 \quad \text{(Equation 25)}$$

The expression of the excitation force F_1 can be obtained by combining the three Equations (20), (24), and (25):

When going down:

$$F_1 = \ddot{x} \cdot \left[m_c + \frac{4\pi^2 \left(J_S + J_{lb} + J_{sb}i_1{}^2 + J_{lg}i_1{}^2 + 2J_{sg1}i_1{}^2 i_2{}^2 + 2J_{mg}i_1{}^2 i_2{}^2 + 2J_{sg2}i^2 + J_g i^2 \right)}{l^2} \right]$$
$$+ \frac{6\pi^2 k_e{}^2 i^2 \dot{x}}{(R_e + R_i) \cdot l^2 \cdot \eta} - m_c g \quad \text{(Equation 26)}$$

When going up:

$$F_1 = \ddot{x} \cdot \left[m_c + \frac{4\pi^2 \left(J_S + J_{lb} + J_{sb}i_1{}^2 + J_{lg}i_1{}^2 + 2J_{sg1}i_1{}^2 i_2{}^2 + 2J_{mg}i_1{}^2 i_2{}^2 + 2J_{sg2}i^2 + J_g i^2 \right)}{l^2} \right]$$
$$+ \frac{6\pi^2 k_e{}^2 i^2 \dot{x}}{(R_e + R_i) \cdot l^2 \cdot \eta} + m_c g \quad \text{(Equation 27)}$$

where, g is the gravitational acceleration;

We introduce the overall friction F_f of the MVR system into the system dynamics. Because the total transmission efficiency is 100%, we can get the final system dynamics equation as follows:

When going down:

$$F = \ddot{x} \cdot \left[m_c + \frac{4\pi^2 \left(J_S + J_{lb} + J_{sb}i_1{}^2 + J_{lg}i_1{}^2 + 2J_{sg1}i_1{}^2 i_2{}^2 + 2J_{mg}i_1{}^2 i_2{}^2 + 2J_{sg2}i^2 + J_g i^2 \right)}{l^2} \right] + \frac{6\pi^2 k_e{}^2 i^2 \dot{x}}{(R_e + R_i) \cdot l^2}$$
$$- m_c g + F_f$$

$$\text{(Equation 28)}$$

When going up:

Table 2. Device parameters

Parameter	Value
Ball screw lead l	40mm
First-stage bevel gear transmission ratio i_1	4
Second-stage spur transmission ratio i_2	4
Third-stage spur transmission ratio i_3	3
The total transmission ratio i	48
The total mass of objects in reciprocating motion m_c	1.716kg
Inertia of ball screw J_S	17.23kg·mm^2
Inertia of large bevel gear J_{lb}	2571kg·mm^2
Inertia of small bevel gear J_{sb}	8.410kg·mm^2
Inertia of large cylindrical spur gear ②J_{lg}	5256kg·mm^2
Inertia of small cylindrical spur gears ① and ③J_{sg1}	20.34kg·mm^2
Inertia of medium cylindrical spur gears ④ and ⑥J_{mg}	1661kg·mm^2
Inertia of small cylindrical spur gears ⑤ and ⑦J_{sg2}	20.34kg·mm^2
Rotational inertia of generator J_g	40kg·mm^2

$$F = \ddot{x} \cdot \left[m_c + \frac{4\pi^2 \left(J_S + J_{lb} + J_{sb} i_1{}^2 + J_{lg} i_1{}^2 + 2J_{sg1} i_1{}^2 i_2{}^2 + 2J_{mg} i_1{}^2 i_2{}^2 + 2J_{sg2} i^2 + J_g i^2 \right)}{l^2} \right] + \frac{6\pi^2 k_e{}^2 i^2 \dot{x}}{(R_e + R_i) \cdot l^2}$$
$$+ m_c g + F_f$$

(Equation 29)

Device parameters are shown in Table 2.

System simulation

Because of the limitation of the experimental equipment, the sinusoidal vibration input was selected for the experiment. Therefore, the system simulation is for sinusoidal input. That is to analyze the changes and differences in the power characteristics and damping force of the MVR harvester under different amplitudes, frequencies, and external load resistances.

When the external load resistance value is set to be 5Ω, the variation of the system damping force under different vibration frequencies and amplitudes is shown in Figure 7. At the same frequency, the damping force of the MVR increases with the amplitude; at the same amplitude, the damping force of the MVR increases with the frequency. Therefore, the damping force is proportional to the vibration frequency and amplitude.

RESULTS AND DISCUSSION
Experiment details

The bench experiments of the MVR were carried out using the MTS Landmark 370.02 servo-hydraulic test system, as shown in Figure 8A. The main parameters of this MTS test system are shown in Table 3 below. The MTS test system controls the vertical position of the lifting beam by the lifting switch to adjust the proposed model in the proper space. When the displacement of the telescopic beam changes, the configured force sensor can record the real-time input force. The upper and lower hydraulic wedge clamps use locking switches to fix the model to keep the model stable during the experiment. The MTS test system also has an emergency stop button to ensure the safety of the whole process of the experiment. Because the vibration frequency of the track is from 1 to 4Hz, the vibration amplitude is between 1 and 12mm (Liu et al., 2017). While verifying the practical feasibility of the MVR proposed in this article, the limitations of the

Simulation results with 1.5Hz, 2Hz and 2.5Hz frequencies.

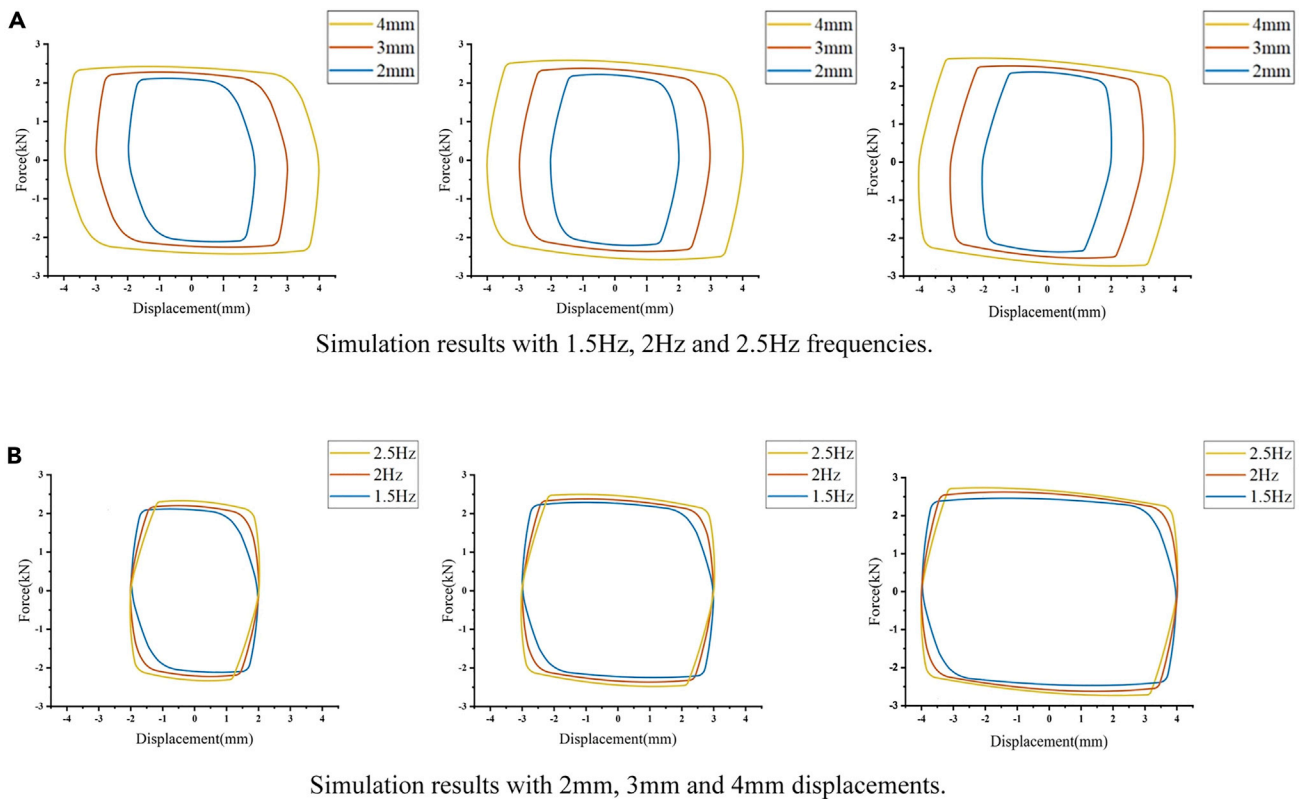Simulation results with 2mm, 3mm and 4mm displacements.

Figure 7. Simulation results of the force-displacement loop
(A) Simulation results with 1.5, 2 and 2.5Hz frequencies.
(B) Simulation results with 2, 3 and 4mm displacements.

experimental equipment should also be considered. Therefore, the experiment was carried out under the condition of a sinusoidal input waveform with a vibration frequency of 1–2.5Hz and an amplitude of 2–4mm.

The on-site layout of the experimental equipment is shown in Figure 8A. The full-scale prototype of the proposed MVR is fixed on the MTS test system, as shown in Figure 8B. Set different parameters and control the start and stop of the experimental bench through the console, as shown in Figure 8C. The displacement and force signals were then measured and recorded with a computer, as shown in Figure 8D. The three-phase generator is connected to three load resistances of equal value, and the resistance values are set to 1, 3, and 5Ω, respectively, as shown in Figure 8E. Finally, the voltage signal of the external load resistor is displayed by an oscilloscope (model RIGOL DS1102Z-E) and stored in the USB flash disk, as shown in Figure 8F.

The field installation details of the MVR under the real track and equipment are shown in Figure 9, including the prototype, oscilloscope, resistors, supercapacitors, a computer, etc. Use an uninterruptible power supply (UPS) to solve the power problem. It shows the layout of MVR in practical application scenarios.

Friction recognition

The experimental determination of the unknown term in Equation (19) is divided into two steps. The first step determines the values of F_f and v under different conditions. The MTS test system is set to excitation with triangular wave displacement (square wave velocity). The generator is always an open circuit, so the force measured at different frequencies and amplitudes is the value of F_f of the MVR. Because the MTS machine is a triangular wave displacement input, the relationship between the square wave velocity and triangular wave displacement is $v = 4 fa$, where f is the frequency and a is the amplitude, thus determining the value of the velocity v. The second step determines the unknowns by fitting the equations. The values of F_f and v of different groups are combined with the least squares method to calculate the value of the unknown
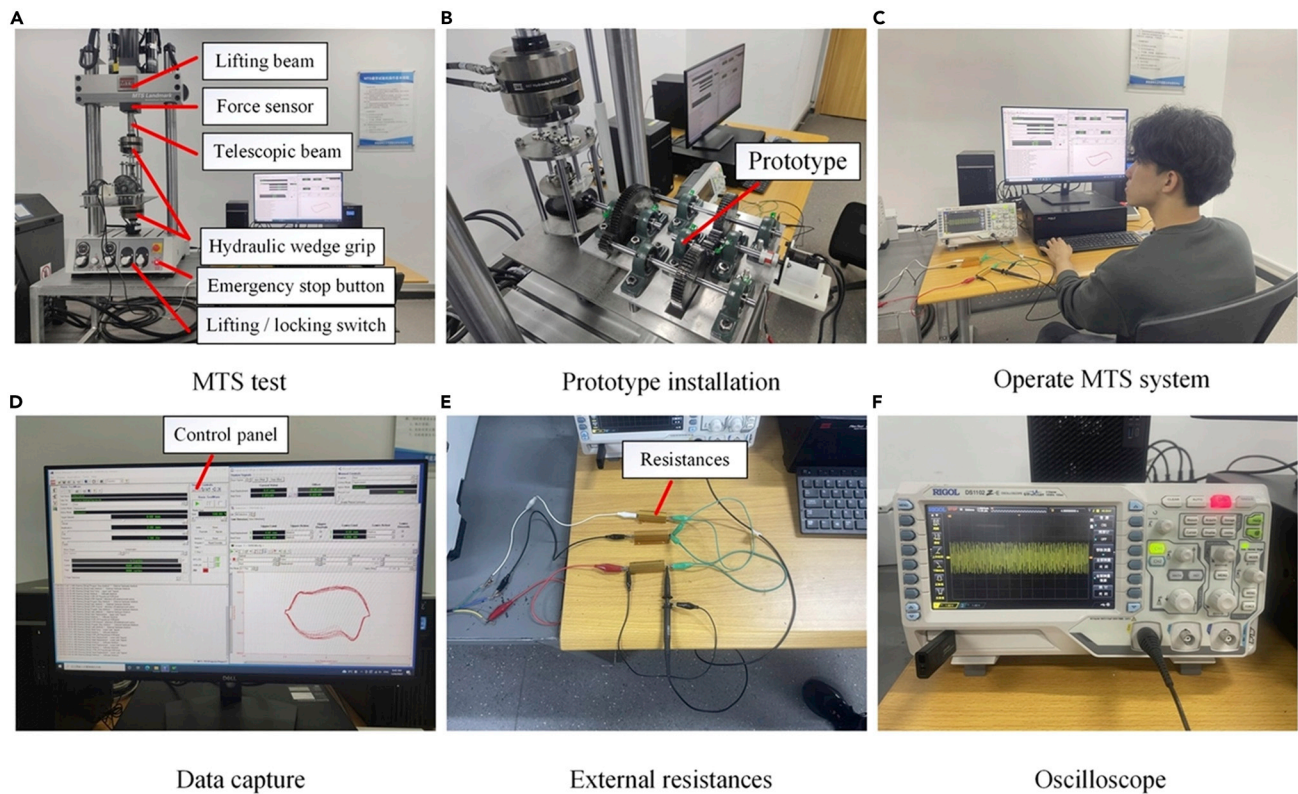
Figure 8. Bench test of the proposed MVR energy harvester
(A) MTS test.
(B) Prototype installation.
(C) Operate MTS system.
(D) Data capture.
(E) External resistances.
(F) Oscilloscope.

parameter in Equation (19). Table 4 lists the average friction and velocity values measured at a frequency of 1.5 Hz at different amplitudes.

Figure 10 shows the input force of the testing machine toward the prototype under the excitation of triangular wave displacement (square wave velocity) at 1.5 Hz. It can be seen that there is still some force fluctuation when the velocity is constant. There are three reasons for this. First, the MVR uses multiple complex transmission components. Because of the precision of processing and assembly, the parts may bounce or misalign, and some

Table 3. Main parameters of MTS Landmark 370.02

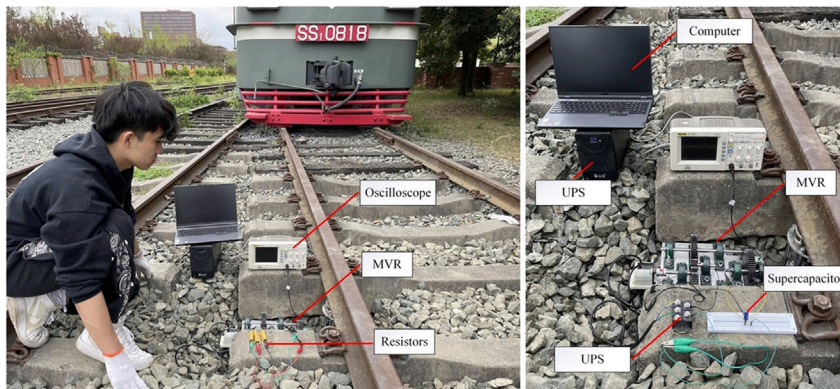| Parameters	Valve	Unit
Test Space Width	460	mm
Test Height Minimum	144	mm
Test Height Maximum	827	mm
Load Frame Rated Capacity	25	kN
Actuator Force Capacity	25	kN
Actuator Dynamic Stroke	150	mm
Actuator Total Stroke	165	mm
Actuator Rated Flow	57	lpm
Manifold Rated Flow	57	lpm

Figure 9. Field installation of MVR under a real track

shocks may occur, resulting in a sudden increase in the force value. Second, the rotational inertia of the transmission system adopted by the MVR is relatively large, which may lead to a certain degree of flywheel effect. Third, because the MTS equipment uses a PID controller, some overshoot and fluctuation will also affect the input force of the MVR, especially when the triangular wave displacement input is used; the sudden change of the driving direction will make this phenomenon more obvious (Li et al., 2020).

Input and output characteristics of the system

The proposed prototype was tested on the MTS test system with a sinusoidal input. In the experiment, the vibration amplitudes are 2, 3, and 4mm, the vibration frequencies are 1, 1.5, 2, and 2.5Hz, and the external loads are 1, 3, and 5Ω. Figure 11 shows the force-displacement loops when the vibration frequency and amplitude are taken as constant values, respectively. The experimental results show that the input force increases when the amplitude or frequency increases. The reason is that when the amplitude or frequency becomes larger, the rotational and linear speed increases, and more kinetic energy needs to be generated to meet the demands of the rotating parts. This means that a larger force needs to be input per unit displacement. In addition, the results also show that the effect of amplitude on the input force is more obvious.

In Figure 12, we analyze the differences between the simulation and experimental results in detail. It can be seen from the comparison that there are five main reasons for the difference between the simulation force-displacement loop and the experimental force-displacement loop. First of all, as shown in mark ①, the experimental value is lower than the simulation value at this time. This is because of the manufacturing and assembly accuracy problems of the MVR, which caused stuck during the experiment, resulting in a low and fluctuating input force. At the position of ②, the force-displacement loop is misaligned, which is caused by the disengagement and engagement under the action of inertia. After the velocity of the input components decreases until it stops, the output rotating components continue to rotate because of inertia and stop later than the input components. When the displacement reaches its maximum value and changes direction, the input components temporarily disengage from the output rotating components. The input force after disengagement drops to a very low value, which results in a large change in amplitude but a small change in force. As shown in mark ③, the area of the experimental force-displacement loop is smaller than that of the simulation force-displacement loop. The reason for this phenomenon is the same as that of ②. Since the disengagement and engagement processes are not considered in the simulation process, the change of the input force is delayed. At the position of ④ in the Figure 12, the value of the experimental force suddenly increases and exceeds the simulation value. This is the result of the combined action of inertia and shock. ④ only appears in the experimental results with higher frequency because the inertia

Table 4. The values of the average friction force and velocity

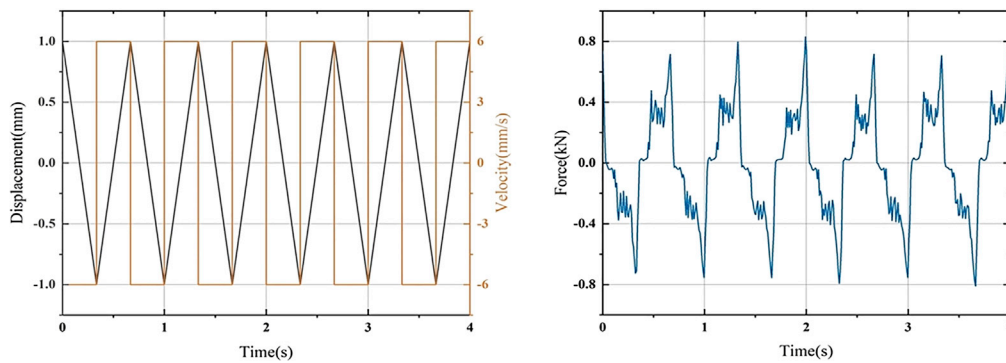| a(mm)	1	1.5	2	2.5	3	3.5	4
v(mm/s)	6	9	12	15	18	21	24
F_f(kN)	0.2854	0.4178	0.5314	0.6287	0.6944	0.7758	0.8245

Figure 10. Displacement, velocity, and Force of the MVR under the excitation of a constant speed with no electric load

effect of the rotating system is more obvious in the high-frequency state, and the faster speed will increase the possibility of shock. In addition, it can be seen that the phenomenon of force fluctuation generally exists in the experimental results, as shown in ⑤. The reason is that the electromagnetic distribution in the generator is not uniform, and the input frequency is low, which causes the damping force to change when the coil cuts off the magnetic induction line (Liu et al., 2017). Although the differences mentioned above exist between the simulation and experimental results, the area range of the force-displacement loop and the magnitude of the force are generally the same. The optimization of the friction model achieves a good match between the simulation and the experiment, and the simulation and experiment force-displacement loops have a high degree of fit. Therefore, it is shown that dynamic models can perform well in predicting MVR performance.

As shown in Figure 13, when the external load resistance is constant at 5Ω, the instantaneous voltage changes with time under different vibrational frequencies and amplitudes. We can see that as the vibration amplitude and vibration frequency increase, the voltage value also increases. In the experimental data, like the influence on the input, the influence of the vibration amplitude on the output voltage is also greater than that of the vibration frequency. The device has a certain flywheel effect, which increases the energy density of the device.
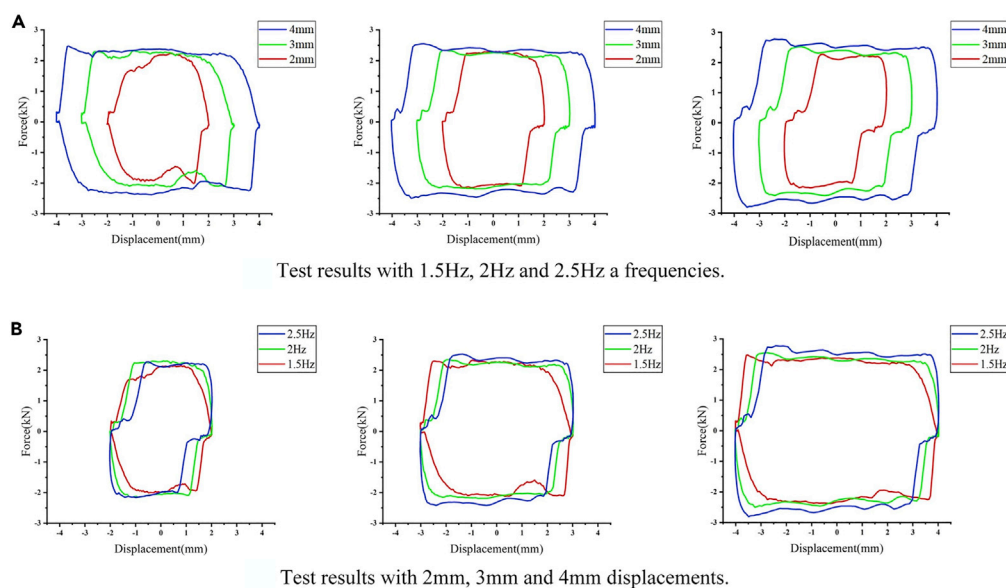
Figure 11. Experimental results of the force-displacement loop
(A) Test results with 1.5, 2 and 2.5Hz a frequencies.
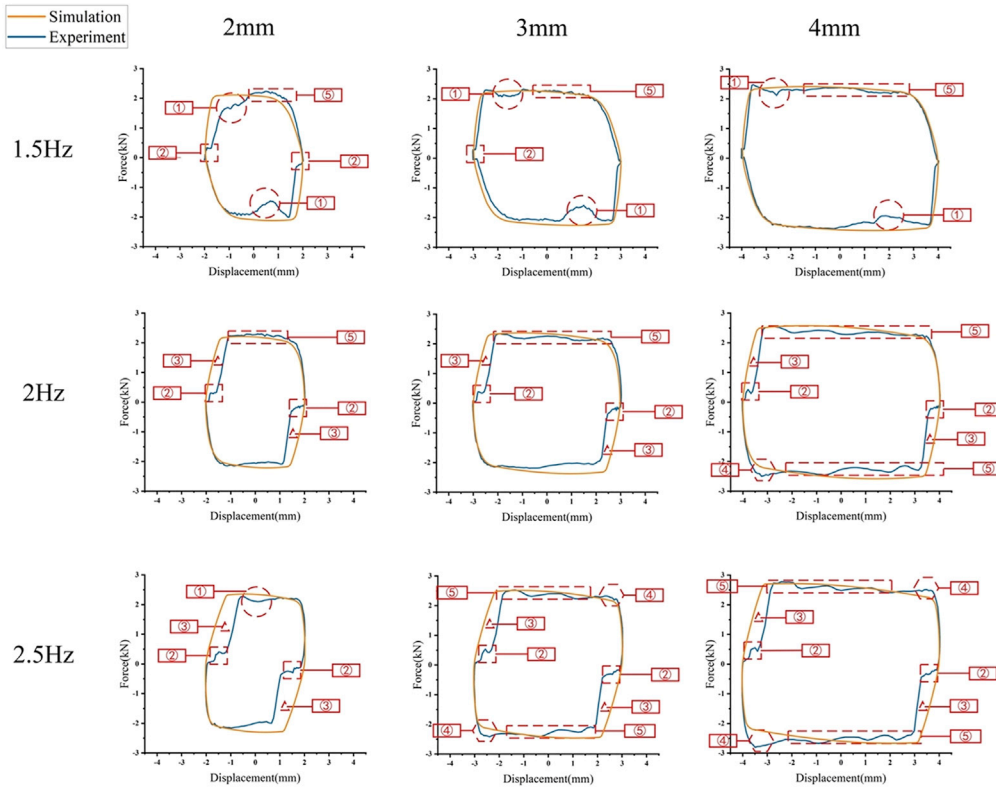(B) Test results with 2, 3 and 4mm displacements.

Figure 12. Comparison of simulation and experimental results

The mechanical efficiency of the MVR is calculated from the experimental data, and the mechanical efficiency of the system is:

$$\eta_m = \frac{W_{output}}{W_{input}} \qquad \text{(Equation 30)}$$

Where W_{input} is calculated from the area surrounded by the experimental force-displacement loop, and W_{output} is calculated from the experimental instantaneous voltage $U(t)$:

$$W_{output} = 3 * \int_0^t \left(U(t)^2 \big/ R_e \right) dt \qquad \text{(Equation 31)}$$

Calculating the output electrical power results of different amplitudes and frequencies and the statistics are shown in Table 5. The output electrical power ranges from a minimum of 6.8988W to a maximum of 28.0416W, and the average mechanical efficiency of the system is 42.73%. It is found that when the external load equals the generator's internal resistance, the load's power reaches the maximum value. It is known that the internal resistance of the generator $R_i = 1.15\Omega$, so when the load resistance gradually approaches the internal resistance $R_i = 1.15\Omega$ from 5 to 3Ω, it finally becomes 1Ω. The output electrical power increases continuously as the load resistance decreases.

Luigi Costanzo et al. introduced an electronic interface for maximizing power extraction from a train suspension energy harvester. A novel maximum power point tracking (MPPT) technique is realized by a DC-DC converter equipped with speed driven adaptive (SDA). Although train vibration characteristics may vary over time, this technique quickly stabilizes the voltage at the rectifier output to an optimum value by measuring the generator velocity in real-time. The SDA technique implements a dynamic adaptive control to handle the tolerances and time variability of the controlled system parameters. Compared with the widely used perturb and observe (P&O), the SDA technique performs better (Costanzo et al., 2021,2020). In the follow-up article, the influence of the voltage drops of the diode bridge rectifier is considered, further optimization is carried out, and a more accurate model is proposed. It is verified experimentally with constant and time-varying generator speeds. In addition, it
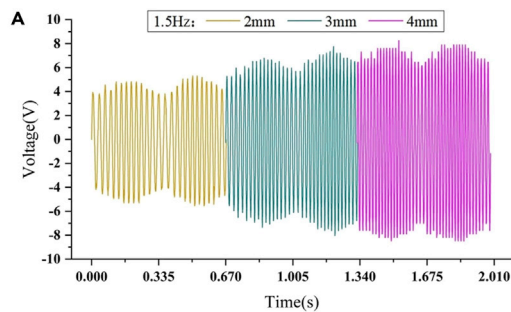
The instantaneous voltage at a frequency of 1.5Hz and an external resistance of 5Ω.
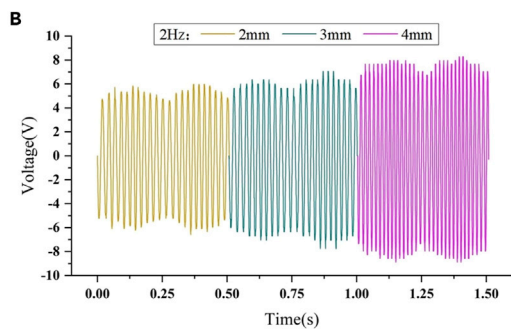
The instantaneous voltage at a frequency of 2Hz and an external resistance of 5Ω.
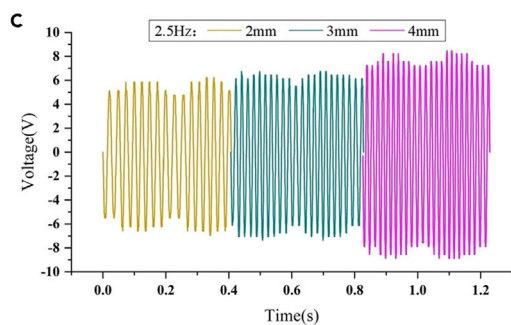
The instantaneous voltage at a frequency of 2.5Hz and an external resistance of 5Ω.

Figure 13. The vibration frequency is 1.5, 2, and 2.5Hz, and the external load is 5Ω
(A) The instantaneous voltage at a frequency of 1.5Hz and an external resistance of 5Ω.
(B) The instantaneous voltage at a frequency of 2Hz and an external resistance of 5Ω.
(C) The instantaneous voltage at a frequency of 2.5Hz and an external resistance of 5Ω.

extends to active AC-DC converters, which have better power extraction performance than passive rectifiers because they can manage both active and reactive power. But more complex control techniques also result in higher control losses relative to passive rectifiers. For both types of converters, the optimal operating conditions for maximum power can be predicted by measuring the generator speed (Costanzo et al., 2022). The proposed system can obtain better output performance if the above optimizations are taken for the energy harvesting circuit in the practical application of MVR.

lot the efficiency values as a three-dimensional curve, as shown in Figure 14 below. The mechanical efficiency is inversely proportional to the vibration amplitude and frequency when the load resistance is constant at 1Ω. And the amplitude change has a more significant effect on the efficiency, as shown in Figure 14A. When the vibration frequency is constant at 2 Hz, the mechanical efficiency generally decreases with the amplitude and load resistance increase. The closer the load resistance is to the internal resistance of the generator, the greater the mechanical efficiency, as shown in Figure 14B. When the vibration amplitude is constant at 2mm, the vibration frequency and load resistance negatively correlate with the

Table 5. Test results with different parameters

Parameters		P_{input} (W)	P_{output} (W)	η_m
1 Ω, 1.5 Hz	2 mm	19.0591	14.4704	75.92%
	3 mm	34.5622	19.4499	56.27%
	4 mm	49.3924	22.2360	45.02%
1Ω, 2Hz	2 mm	27.4008	20.1766	73.64%
	3 mm	41.7477	21.3313	53.23%
	4 mm	61.3407	25.5045	41.58%
1Ω, 2.5Hz	2 mm	28.7088	20.3981	71.05%
	3 mm	52.1211	25.6695	49.25%
	4 mm	74.1720	28.0416	37.81%
3 Ω, 1.5 Hz	2 mm	21.9739	11.3101	51.47%
	3 mm	38.5166	15.7362	40.86%
	4 mm	44.5195	21.7536	48.86%
3Ω, 2Hz	2 mm	32.5796	15.6864	48.15%
	3 mm	51.2587	17.6174	34.37%
	4 mm	61.5516	23.0778	37.49%
3Ω, 2.5Hz	2 mm	39.0293	17.4858	44.80%
	3 mm	64.3221	19.5774	30.44%
	4 mm	74.4570	22.3908	30.07%
5 Ω, 1.5 Hz	2 mm	19.0571	6.8988	36.20%
	3 mm	32.9313	12.6582	38.44%
	4 mm	48.7205	18.0378	37.02%
5Ω, 2Hz	2 mm	28.0438	9.6613	34.45%
	3 mm	45.5547	13.0674	28.69%
	4 mm	67.4910	19.8708	29.44%
5Ω, 2.5Hz	2 mm	31.9264	10.9188	34.20%
	3 mm	59.9067	13.5678	22.65%
	4 mm	91.7458	20.4006	22.24%

mechanical efficiency. And the change in load resistance has a greater impact on efficiency currently, as shown in Figure 14C. In general, the mechanical efficiency of MVR increases with the decrease of vibration amplitude, vibration frequency, and load resistance in the experimental data.

Charging experiment and application analysis

The MTS bench test using MVR to charge supercapacitors is shown in Figure 15. The test adopts the vibration condition of the lowest frequency and the smallest amplitude: the vibration frequency is 1.5Hz, and the vibration amplitude is 2mm. Using the smallest data can better prove the feasibility of the MVR to charge the supercapacitor and power the tracking sensor network. The capacitances are 1, 1.65 and 2.5F, respectively. With the same output voltage, in theory, the final voltage of the supercapacitor can be the same. But the test results show that the charging voltage of the supercapacitor can first rise rapidly to a certain value and then slowly rise to the final value. It can also be seen from Figure 15 that different capacitances have a different time to reach the same charging voltage. As the capacitance increases, so does time. In general, the fast-charging characteristics and large-capacity characteristics of supercapacitors provide the necessary guarantee for the self-power of sensor networks.

To ensure the safety and feasibility of the device, a comparative analysis is made on whether the proposed energy harvester is installed on the track. The experimental data uses the experimental displacement responses recorded by the MTS test system. Among them, the data adopts the largest data in this experiment; the vibration frequency is 2.5Hz, the amplitude is 4mm, and the external load is 5Ω for testing.
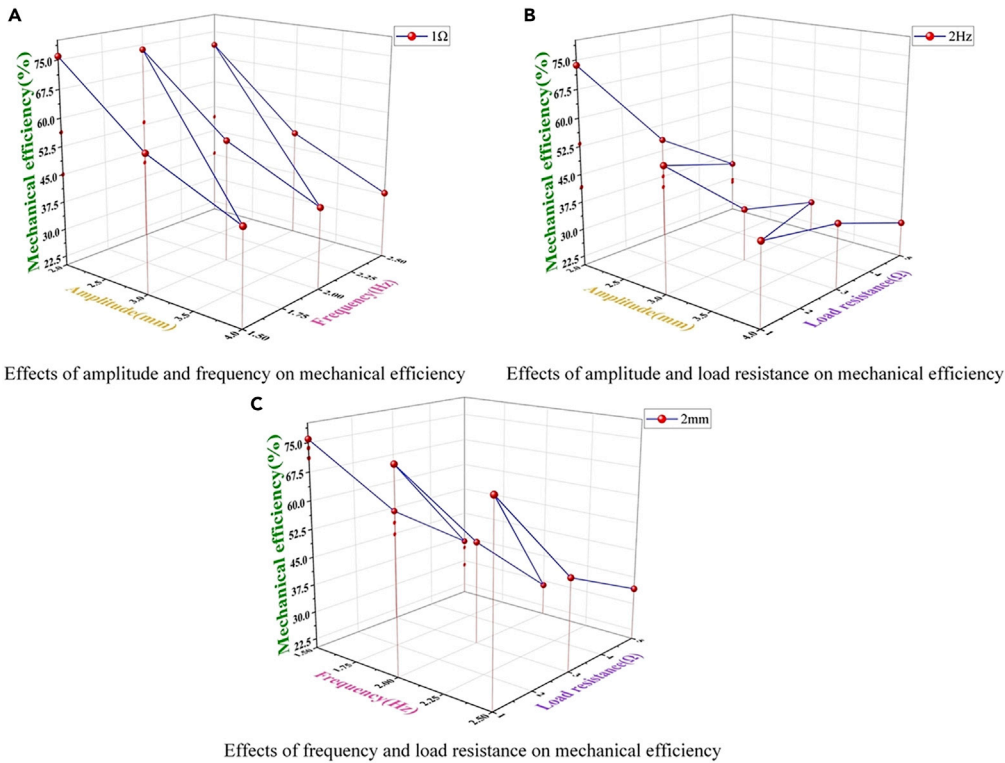
Figure 14. Mechanical efficiency of MVR
(A) Effect of amplitude and frequency on mechanical efficiency.
(B) Effect of amplitude and load resistance on mechanical efficiency.
(C) Effect of frequency and load resistance on mechanical efficiency.

Therefore, the safety of the device can be better proved. From Figure 16, it can be concluded that the presence or absence of MVR has very little effect on the track. In addition, comparing the vibration data after installing the MVR with the original vibration data, the mean relative error (MRE) was 0.0125%. The
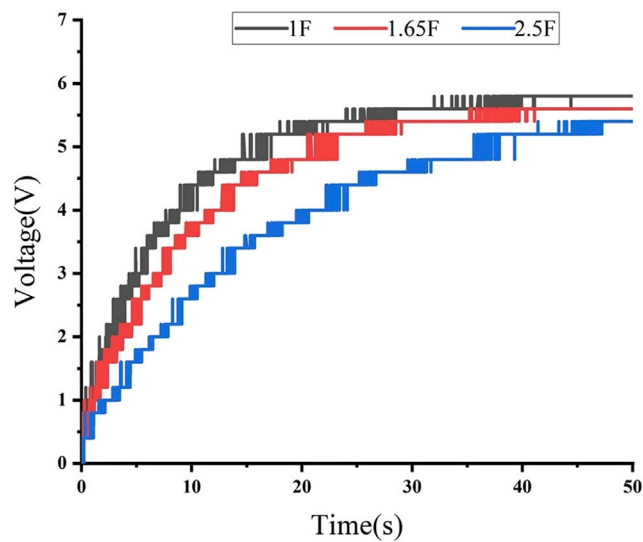
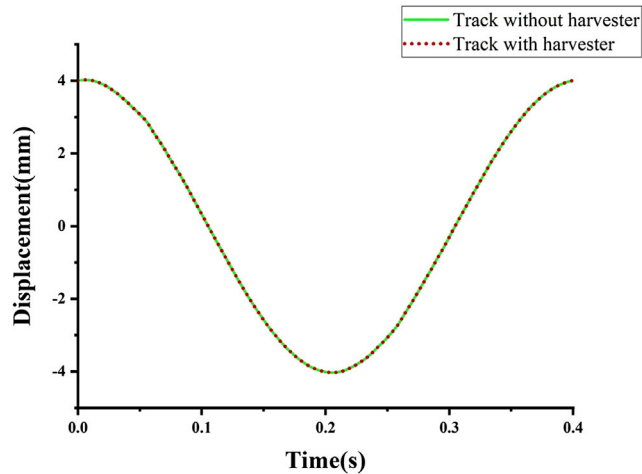

Figure 15. Charging test of MVR

Figure 16. Track displacement with and without a harvester

installation of MVR will not affect the dynamic response of the train, nor will it bring any safety problems to the train operation.

Figure 17 shows the practical application of the proposed MVR in a heavy-duty freight train railway. When a freight train passes, the contact between the wheels and the track will cause irregular reciprocating vibrations. The MVR harvests the track vibration energy that would otherwise be wasted through rectification and voltage regulation processing to achieve the purpose of power generation. The electrical energy stored in the supercapacitor powers low-power wireless sensors such as tilt sensors, acceleration sensors, gyroscope sensors, and displacement sensors. The sensor transmits the track safety information monitored in real-time to the remote monitoring terminal through the wireless sensor network, signal processing, satellite transmission, and other processes and keep information interaction with freight trains at all times. If there is a safety problem on the track, the train driver can be notified via satellite to avoid safety accidents. In addition, there are two energy supplies for the sensor: battery and grid. In some remote areas, the battery needs to be replaced manually and regularly, and it will cause a certain degree of pollution to the environment. Laying the power grid consumes a lot of manpower and material resources, and long-distance power transmission will also cause power loss. Through harvesting track vibration energy, the self-power of low-power wireless sensors is realized. The MVR feeds back the energy from the track to the safety monitoring of the track to ensure the stable and safe operation of the freight train. Therefore, the MVR proposed in this article, applied to wireless sensor self-powered and freight train track safety monitoring, has huge economic benefits and application value.

Figure 17. Application of MVR in freight railway

Table 6. Several track wireless sensor parameters

Sensor model	Category	Range	Power consumption	Size	manufacturer
TS1010T	Inclination	$\pm 10g$	10mW	8.9 × 8.9 × 3.24mm	Colibrys
VS1200.A	Acceleration	$\pm 100g$	10.24mW	8.9 × 8.9 × 3.24mm	Colibrys
Z4D-C01	Displacement	$6.5 \pm 1mm$	70mW	35.5 × 16 × 15mm	Omron
P8AP	Pressure	500bar	390mW	Φ10 × 114mm	HBM
VY4	Strain	Nominal resistance 350Ohm	100mW	9.8 × 10mm	HBM
RDS40	Crack	Rated resistance 28Ohm	250mW	47 × 10mm	HBM
CRG20-02	Gyroscope	$\pm 300°/s$	<300mW	9.5 × 9 × 3.44mm	Silicon Sensing
SHT31	Temperature and humidity	0–100%RH;-40–125°C	4.8μW	2.5 × 2.5 × 0.9mm	SENSIRION

From Ref (Pan et al., 2019a), it can be known that the vibration range of the track is 1–12mm and 1-4Hz, and the specific situation is related to the train type and load. This article studies heavy-duty tracks for freight trains. Because of equipment limitations, etc., the 2-4mm and 1.5–2.5Hz used in the experiment are the smaller values in the track vibrations. In heavy-duty track conditions, the MVR will generate more power. Therefore, it is of great reference value to use the average power under the condition of 2.5Hz as the estimation of power generation. Track wireless sensor systems often include tilt, acceleration, displacement, and pressure sensors. The combined power of these sensors is 0.48W. Table 6 lists the parameters of several other common track monitoring wireless sensors. The average power is 24.7029W when the load is 1Ω, and the vibration frequency is 2.5Hz. Assuming that the speed of the freight train is 60 km/h, the fixed wheelbase of the bogie is 1800mm, the diameter of the upper roof is 120mm, the action time of one carriage on the MVR is 0.1152s, the number of carriages is 100, and the number of trains passing through each day is 24. To fully harvest the track vibration energy, 20 proposed MVRs are arranged on opposite sides of the track. When all trains in a day pass by the MVRs, the total power generation is 136.60kJ. The combination of four common track-side wireless sensors: tilt sensor, acceleration sensor, displacement sensor, and pressure sensor, can be continuously powered for 70.05h >24 h. It can realize the all-day power supply to the sensor combination. This is the case where the vibration amplitude and frequency are smaller than the actual vibration of the track, and only 10 MVRs are arranged on one side of the track. If the proposed MVRs are installed on a large scale, a higher power generation will be achieved, which can fully realize the self-powered wireless sensor networks.

Table 7 summarizes the electromagnetic vibration energy harvester systems proposed in the railway field. The mechanism, installation location, electrical performance, and efficiency are compared. All prototypes and data are from the corresponding literature. From the installation position, the output power of the devices on the track-side is significantly higher than that of the onboard devices, but the efficiency is lower. However, MVR has improved in efficiency compared to track-side or onboard devices. At the same time, its output power is also higher in the track-side devices. In contrast, it can be seen that the proposed MVR in this article has better electrical performance and energy conversion efficiency.

Conclusions

This article proposes a track vibration energy harvesting system with a MVR mechanism as the core. The motion conversion module and the motion rectification module of the device are arranged vertically to avoid excessive length, which is beneficial to the installation of the device. The mechanism of the MVR adopts a design that combines the bevel gear speed increase and the spur gear multi-stage speed increase. This can fully use the large input force of the track vibration and harvest the track vibration energy to a greater extent. The system includes four modules: motion conversion, rectification, generator, and storage. The motion conversion module converts the linear vibration of the track into the bidirectional rotation of the bevel gear through the ball screw. The motion rectification module converts the bidirectional rotation of the bevel gear into a faster unidirectional rotation of the generator shaft by integrating mechanical rectification and speed increase. Then, the three-phase brushless generator generates electrical energy. After the rectification and voltage regulation, the electrical energy will be stored in the

Table 7. Comparison of electromagnetic energy harvesters in railway systems

No	Reference	Harvester mechanism	Installation position	Input	Voltage	Power	Efficiency
On-board							
1	(dePasquale et al., 2012)	Magnetic suspension	Wheelset axle box	80 km/h	2.5 V (Vmax)	100 mW (Pmax)	/
2	(Ung et al., 2015)	Inertial mass	wagon	4.16 m/s^{-2}	/	1.71 mW (Pmax)	/
3	(Ung et al., 2016)	Inertial pendulum	Suspension	3.92 m/s^{-2}	/	200 mW (Pmax)	/
4	(Brignole et al., 2016)	Resonant electromagnetic	Bogie	75 km/h	/	2.7 mW (Pmax)	/
5	(Bradai et al., 2018)	Magnetic spring	wagon	27 Hz	1.7 V (Vp-p)	10 mW (Pmax)	/
6	(Gao et al., 2020)	Inertial pendulum	Bogie	80 km/h	1.45 V (Vrms)	263 mW (Prms)	65%
7	(Perez et al., 2020)	Inertial mass	Bogie	28 Hz, 40 Hz	/	6.5 mW (Pavg)	/
8	(Fang et al., 2022)	Inertial pendulum	Bogie	120 km/h	1.5 V (Vp-p)	102 mW (Prms)	68.29%
Track-side							
9	(Wang et al., 2012)	Double rack and pinion set	Track-side	0.5 inch, 1 Hz	5 V (Vp-p)	1.4 W (Pmax)	16.9%
10	(Zhang et al., 2016)	Rack and pinion	Track-side	2Hz, 6mm	6.45 V (Vp-p)	36.5 mW (Pavg)	55.5%
11	(Gao et al., 2018b)	Magnetic suspension	Track-side	105 km/h	2.3 V (Vp-p)	119 mW (Pmax)	/
12	(Gao et al., 2018a)	Magnetic suspension	Track-side	7–500 Hz	6.96 V (Vp-p)	550 mW (Pmax)	60%
13	(Dotti and Sosa, 2019)	Inertial pendulum	Track-side	0.5 kg	/	5–6 W (Pavg)	/
14	(Pan et al., 2019a)	Ball screw bevel gear set	Track-side	30 km/h	/	2.24 W (Pavg)	/
15	(Wu et al., 2021)	Ball screw bevel gear set	Track-side	2 Hz, 7.5 mm	4 V (Vavg)	5.3 W (Pavg)	55.4%
16	This work	Ball screw bevel gear set	Track-side	2.5Hz, 4mm	17.42 V (Vp-p)	28.04 W (Pavg)	75.92%

supercapacitor and supplied to the track-side wireless sensor systems. The performance and dynamic response of the proposed device are verified by simulation and experimental analysis.

The proposed MVR adopts sinusoidal input in the MTS bench experiment. When the amplitude is 4mm, the frequency is 2.5Hz, and the external load is 1Ω, the power can reach 28.0416W. The highest mechanical efficiency is 75.92%, and its average value is 42.73%. Because of the heavy load conditions of freight train tracks, the proposed MVR has great potential for power generation. The realization of low-power wireless sensor self-energy can ensure the safe operation of freight trains and contribute to green energy development, carbon neutrality, emission reduction, and environmental protection.

Limitations of the study

The proposed vibration energy harvesting system still needs further optimization analysis and field experiments. The limitations of this study are summarized as follows:

(1) Because of experimental conditions and equipment limitations, the simulation and experiment use a regular sine wave input. To more accurately evaluate the performance of the proposed system, future studies will be tested on real-running tracks.

(2) Start the finite element analysis and fatigue testing of the proposed system and further improve the machining and fitting accuracy of the device to predict and improve the life of the device.

(3) Clean energy such as solar, wind, and noise are also included along the freight train track. Therefore, there is great potential to explore the form of hybrid energy harvesting as a supplementary energy source for MVR.

STAR★METHODS

Detailed methods are provided in the online version of this paper and include the following:

- KEY RESOURCES TABLE

- ● RESOURCE AVAILABILITY
  - ○ Lead contact
  - ○ Material availability
  - ○ Data and code availability
- ● METHOD DETAILS
- ● QUANTIFICATION AND STATISTICAL ANALYSIS

AUTHOR CONTRIBUTIONS

G.L: Conceptualization, methodology, software, validation, and writing – original draft; Z.F: Validation, software, and resources; Z.Z: Corresponding author, writing – review and editing; X.T: Data curation and methodology; C.D: Investigation and validation; X.W: Writing – review and editing; Z.J: Formal analysis and validation; D.L: Investigation and resources.

DECLARATION OF INTERESTS

The author declares no competing interests.

REFERENCES

Abido, M.Y., Mahmud, Z., Sánchez-Pérez, P.A., and Kurtz, S.R. (2022). Seasonal challenges for a California renewable- energy-driven grid. iScience 25, 103577. https://doi.org/10.1016/j.isci.2021.103577.

Armstrong-Hélouvry, B., Dupont, P., and de Wit, C.C. (1994). A survey of models, analysis tools and compensation methods for the control of machines with friction. Automatica 30, 1083–1138. https://doi.org/10.1016/0005-1098(94)90209-7.

Bradai, S., Naifar, S., Viehweger, C., and Kanoun, O. (2018). Electromagnetic vibration energy harvesting for railway applications. MATEC Web of Conferences 148, 12004. https://doi.org/10.1051/matecconf/201814812004.

Brignole, O., Cavalletti, C., Maresca, A., Mazzino, N., Balato, M., Buonomo, A., Costanzo, L., Giorgio, M., Langella, R., Schiavo, A.L., Testa, A., and Vitelli, M. (2016). Resonant electromagnetic vibration harvesters feeding sensor nodes for real-time diagnostics and monitoring in railway vehicles for goods transportation: a numerical-experimental analysis. In 2016 IEEE International Power Electronics and Motion Control Conference (PEMC) (IEEE), pp. 456–461. https://doi.org/10.1109/EPEPEMC.2016.7752040.

Cañete, E., Chen, J., Díaz, M., Llopis, L., and Rubio, B. (2015). Sensor4PRI: a sensor platform for the protection of railway infrastructures. Sensors 15, 4996–5019. https://doi.org/10.3390/s150304996.

Cao, H., Wu, X., Wu, H., Pan, Y., Luo, D., Azam, A., and Zhang, Z. (2022). A hybrid self-powered system based on wind energy harvesting for low-power sensors on canyon bridges. Int. J. Precis. Eng. Manuf. Green Technol. https://doi.org/10.1007/s40684-022-00424-0.

Costanzo, L., Vitelli, M., lo Schiavo, A., and Zuo, L. (2020). Optimization of diode bridge rectifier output voltage in Train Suspension Energy Harvesters. In 2020 IEEE 20th Mediterranean Electrotechnical Conference (MELECON) (IEEE), pp. 197–201. https://doi.org/10.1109/MELECON48756.2020.9140723.

Costanzo, L., Lin, T., Lin, W., Schiavo, A.L., Vitelli, M., and Zuo, L. (2021). Power electronic interface with an adaptive MPPT technique for train suspension energy harvesters. IEEE Trans. Ind. Electron. 68, 8219–8230. https://doi.org/10.1109/TIE.2020.3009584.

Costanzo, L., Schiavo, A.L., Vitelli, M., and Zuo, L. (2022). Optimization of AC–DC converters for regenerative train suspensions. IEEE Trans. Ind. Appl. 58, 2389–2399. https://doi.org/10.1109/TIA.2021.3136145.

de Pasquale, G., Somà, A., and Zampieri, N. (2012). Design, simulation, and testing of energy harvesters with magnetic suspensions for the generation of electricity from freight train vibrations. J. Comput. Nonlinear Dynam. 7. https://doi.org/10.1115/1.4006920.

Dotti, F.E., and Sosa, M.D. (2019). Pendulum systems for harvesting vibration energy from railroad tracks and sleepers during the passage of a high-speed train: a feasibility evaluation. Theor. Appl. Mech. Lett. 9, 229–235. https://doi.org/10.1016/j.taml.2019.03.005.

Dupont, P., Hayward, V., Armstrong, B., and Altpeter, F. (2002). Single state elastoplastic friction models. IEEE Trans. Automat. Control 47, 787–792. https://doi.org/10.1109/TAC.2002.1000274.

Fang, Z., Tan, X., Liu, G., Zhou, Z., Pan, Y., Ahmed, A., and Zhang, Z. (2022). A novel vibration energy harvesting system integrated with an inertial pendulum for zero-energy sensor applications in freight trains. Appl. Energy 318, 119197. https://doi.org/10.1016/j.apenergy.2022.119197.

Gao, M., Wang, P., Cao, Y., Chen, R., and Cai, D. (2016). Design and verification of a rail-borne energy harvester for powering wireless sensor networks in the railway industry. IEEE Trans. Intell. Transport. Syst. 1–14. https://doi.org/10.1109/TITS.2016.2611647.

Gao, M., Li, Y., Lu, J., Wang, Y., Wang, P., and Wang, L. (2018a). Condition monitoring of urban rail transit by local energy harvesting. Int. J.

Distributed Sens. Netw. *14*. 155014771881446. https://doi.org/10.1177/1550147718814469.

Gao, M., Wang, P., Wang, Y., and Yao, L. (2018b). Self-powered ZigBee wireless sensor nodes for railway condition monitoring. IEEE Trans. Intell. Transport. Syst. *19*, 900–909. https://doi.org/10.1109/TITS.2017.2709346.

Gao, M., Cong, J., Xiao, J., He, Q., Li, S., Wang, Y., Yao, Y., Chen, R., and Wang, P. (2020). Dynamic modeling and experimental investigation of self-powered sensor nodes for freight rail transport. Appl. Energy *257*, 113969. https://doi.org/10.1016/j.apenergy.2019.113969.

Hao, D., Qi, L., Tairab, A.M., Ahmed, A., Azam, A., Luo, D., Pan, Y., Zhang, Z., and Yan, J. (2022). Solar energy harvesting technologies for PV self-powered applications: a comprehensive review. Renew. Energy *188*, 678–697. https://doi.org/10.1016/j.renene.2022.02.066.

Hodge, V.J., O'Keefe, S., Weeks, M., and Moulds, A. (2015). Wireless sensor networks for condition monitoring in the railway industry: a survey. IEEE Trans. Intell. Transport. Syst. *16*, 1088–1106. https://doi.org/10.1109/TITS.2014.2366512.

Jin, J.-W., Kang, K.-W., and Kim, J.-H. (2015). Development of durability test procedure of vibration-based energy harvester in railway vehicle. Int. J. Precis. Manuf. Green Technol. *2*, 353–358. https://doi.org/10.1007/s40684-015-0043-6.

Jin, L., Deng, W., Su, Y., Xu, Z., Meng, H., Wang, B., Zhang, H., Zhang, B., Zhang, L., Xiao, X., Zhu, M., and Yang, W. (2017). Self-powered wireless smart sensor based on maglev porous nanogenerator for train monitoring system. Nano Energy *38*, 185–192. https://doi.org/10.1016/j.nanoen.2017.05.018.

Kim, S.-C., Kim, J.-G., Kim, Y.-C., Yang, S.-J., and Lee, H. (2019). A study of electromagnetic vibration energy harvesters: design optimization and experimental validation. Int. J. Precis. Eng. Manuf. Green Technol. *6*, 779–788. https://doi.org/10.1007/s40684-019-00130-4.

Li, X., Chen, C., Li, Q., Xu, L., Liang, C., Ngo, K., Parker, R.G., and Zuo, L. (2020). A compact mechanical power take-off for wave energy converters: design, analysis, and test verification. Appl. Energy *278*, 115459. https://doi.org/10.1016/j.apenergy.2020.115459.

Li, N., Jia, C., Fang, Z., Jiang, Z., Ahmed, A., Hao, D., Zhang, Z., and Luo, D. (2022). A U-shaped kinetic energy harvester for application in a near-zero energy parking system. Sustain. Cities Soc. *81*, 103866. https://doi.org/10.1016/j.scs.2022.103866.

Lin, T., Pan, Y., Chen, S., and Zuo, L. (2018). Modeling and field testing of an electromagnetic energy harvester for rail tracks with anchorless mounting. Appl. Energy *213*, 219–226. https://doi.org/10.1016/j.apenergy.2018.01.032.

Liu, Y., Xu, L., and Zuo, L. (2017). Design, modeling, lab, and field tests of a mechanical-

motion-rectifier-based energy harvester using a ball-screw mechanism. IEEE ASME Trans. Mechatron. *22*, 1933–1943. https://doi.org/10.1109/TMECH.2017.2700485.

Liu, J., Peng, Q., Huang, Z., Liu, W., and Li, H. (2018). Enhanced sliding mode control and online estimation of optimal slip ratio for railway vehicle braking systems. Int. J. Precis. Eng. Manuf. *19*, 655–664. https://doi.org/10.1007/s12541-018-0079-y.

Pan, Y., Lin, T., Qian, F., Liu, C., Yu, J., Zuo, J., and Zuo, L. (2019a). Modeling and field-test of a compact electromagnetic energy harvester for railroad transportation. Appl. Energy *247*, 309–321. https://doi.org/10.1016/j.apenergy.2019.03.051.

Pan, Y., Liu, F., Jiang, R., Tu, Z., and Zuo, L. (2019b). Modeling and on-board test of an electromagnetic energy harvester for railway cars. Appl. Energy *250*, 568–581. https://doi.org/10.1016/j.apenergy.2019.04.182.

Park, H. (2017). Vibratory electromagnetic induction energy harvester on wheel surface of mobile sources. Int. J. Precis. Eng. Manuf. Green Technol. *4*, 59–66. https://doi.org/10.1007/s40684-017-0008-z.

Penalba, M. (2018). A high-fidelity wave-to-wire simulation platform for wave energy converters: Coupled numerical wave tank and power take-off models. Appl. Energy *226*, 655–669. https://doi.org/10.1016/j.apenergy.2018.06.008.

Perez, M., Chesné, S., Jean-Mistral, C., Billon, K., Augez, R., and Clerc, C. (2020). A two degree-of-freedom linear vibration energy harvester for tram applications. Mech. Syst. Signal Process. *140*, 106657. https://doi.org/10.1016/j.ymssp.2020.106657.

Pourghodrat, A., Nelson, C.A., Phillips, K.J., and Fateh, M. (2011). Improving an energy harvesting device for railroad safety applications, M.N. Ghasemi-Nejhad, ed., p. 79770U. https://doi.org/10.1117/12.880631.

Pourghodrat, A., Nelson, C.A., Hansen, S.E., Kamarajugadda, V., and Platt, S.R. (2014). Power harvesting systems design for railroad safety. Proc. Inst. Mech. Eng. - Part F J. Rail Rapid Transit *228*, 504–521. https://doi.org/10.1177/0954409713482659.

Qi, L., Pan, H., Pan, Y., Luo, D., Yan, J., and Zhang, Z. (2022). A review of vibration energy harvesting in rail transportation field. iScience *25*, 103849. https://doi.org/10.1016/j.isci.2022.103849.

Schismenos, S., Chalaris, M., and Stevens, G. (2021). Battery hazards and safety: a scoping review for lead acid and silver-zinc batteries. Saf. Sci. *140*, 105290. https://doi.org/10.1016/j.ssci.2021.105290.

Ung, C., Moss, S.D., Chiu, W.K., Payne, O.R., Vandewater, L.A., and Galea, S.C. (2015). In In-service demonstration of electromagnetic vibration energy harvesting technologies for heavy haul rail applications, K.M. Farinholt and

S.F. Griffin, eds., p. 94330Z. https://doi.org/10.1117/12.2084424.

Ung, C., Moss, S.D., and Chiu, W.K. (2016). Vibration energy harvesting from heavy haul railcar vibrations using a two-degree-of-freedom coupled oscillating system. Proc. Inst. Mech. Eng. - Part F J. Rail Rapid Transit *230*, 924–934. https://doi.org/10.1177/0954409715569861.

Wang, J.J., Penamalli, G.P., and Zuo, L. (2012). Electromagnetic energy harvesting from train induced railway track vibrations. In Proceedings of 2012 IEEE/ASME 8th IEEE/ASME International Conference on Mechatronic and Embedded Systems and Applications (IEEE), pp. 29–34. https://doi.org/10.1109/MESA.2012.6275532.

Wang, Y., Zhu, X., Zhang, T., Bano, S., Pan, H., Qi, L., Zhang, Z., and Yuan, Y. (2018). A renewable low-frequency acoustic energy harvesting noise barrier for high-speed railways using a Helmholtz resonator and a PVDF film. Appl. Energy *230*, 52–61. https://doi.org/10.1016/j.apenergy.2018.08.080.

Wu, X., Qi, L., Zhang, T., Zhang, Z., Yuan, Y., and Liu, Y. (2021). A novel kinetic energy harvester using vibration rectification mechanism for self-powered applications in railway. Energy Convers. Manag. *228*, 113720. https://doi.org/10.1016/j.enconman.2020.113720.

Xie, Q., Zhang, T., Pan, Y., Zhang, Z., Yuan, Y., and Liu, Y. (2020). A novel oscillating buoy wave energy harvester based on a spatial double X-shaped mechanism for self-powered sensors in sea-crossing bridges. Energy Convers. Manag. *204*, 112286. https://doi.org/10.1016/j.enconman.2019.112286.

Yu, J., Saydaliev, H.B., Liu, Z., Nazar, R., and Ali, S. (2022). The asymmetric nexus of solar energy and environmental quality: evidence from Top-10 solar energy-consuming countries. Energy *247*, 123381. https://doi.org/10.1016/j.energy.2022.123381.

Zhang, X., Zhang, Z., Pan, H., Salman, W., Yuan, Y., and Liu, Y. (2016). A portable high-efficiency electromagnetic energy harvesting system using supercapacitors for renewable energy applications in railroads. Energy Convers. Manag. *118*, 287–294. https://doi.org/10.1016/j.enconman.2016.04.012.

Zhang, T., Wu, X., Pan, Y., Luo, D., Xu, Y., Zhang, Z., Yuan, Y., and Yan, J. (2022). Vibration energy harvesting system based on track energy-recycling technology for heavy-duty freight railroads. Appl. Energy *323*, 119673. https://doi.org/10.1016/j.apenergy.2022.119673.

Zhao, X., Wei, G., Li, X., Qin, Y., Xu, D., Tang, W., Yin, H., Wei, X., and Jia, L. (2017). Self-powered triboelectric nano vibration accelerometer based wireless sensor system for railway state health monitoring. Nano Energy *34*, 549–555. https://doi.org/10.1016/j.nanoen.2017.02.036.

STAR★METHODS

KEY RESOURCES TABLE

REAGENT or RESOURCE	SOURCE	IDENTIFIER
Software and algorithms		
Microsoft Visio 2016	Microsoft	https://www.microsoft.com/zh-cn/microsoft-365/visio/flowchart-software
MATLAB 2020b	Mathworks	https://www.mathworks.com/products/matlab.html
Other		
MTS Landmark 370.02 servo-hydraulic test system	Mechanical Testing and Sensing (MTS) Systems Corporation	https://www.mts.com/en/products/materials/dynamic-materials-test-systems/landmark-servohydraulic
DS1102Z-E digital oscilloscope	RIGOL	https://rigol.com

RESOURCE AVAILABILITY

Lead contact

Further information and requests for resources and reagents should be directed to and will be fulfilled by the lead contact Zutao Zhang (zzt@swjtu.edu.cn).

Material availability

This study did not generate new unique reagents.

Data and code availability

- All data reported in this paper will be shared by the lead contact upon reasonable request.

- This paper does not report the original code.

- Any additional information required to reanalyze the data reported in this paper is available from the lead contact upon request.

METHOD DETAILS

All methods can be found in the main text. Please check the System design section for the design details of the system. Please check the Dynamic analysis and simulation section for the simulation and analysis details of the system. Please refer to the Experimental details section for details of the experimental design and equipment performance parameters.

Microsoft Visio 2016 is used to generate the visual images in the manuscript. MATLAB 2020b is used to process experimental data and generate visual images in the manuscript. A demo video is provided to introduce the whole article more vividly, as shown in Video S1.

QUANTIFICATION AND STATISTICAL ANALYSIS

Microsoft Visio 2016 is used to generate the visual images in the manuscript. The voltage signals are captured by the DS1102Z-E digital oscilloscope. The force-displacement signals are captured by the force sensor and displacement sensors integrated into the Landmark 370 servo-hydraulic test system at a sampling frequency of 300 Hz. MATLAB 2020b is used to process experimental data and generate visual images in the manuscript. Through MATLAB 2020b, the voltage signal and force-displacement data are processed to analyze the input and output characteristics of the system.